ARTICLE OPEN

Check for updates

Role of MnS in the intergranular corrosion and depassivation of sensitized Type 304 stainless steel

Noriyuki Ida[1,2], Masashi Nishimoto [1 ✉], Izumi Muto [1 ✉] and Yu Sugawara [1]

During polarization in 1 M NaCl (pH 5.4), intergranular corrosion of sensitized re-sulfurized Type 304 stainless steel occurred after pit initiation at MnS inclusions. Intergranular corrosion occurred when the pitting corrosion reached a Cr-depleted region along the sensitized grain boundaries. During depassivation under open-circuit conditions in 1 M NaCl (pH 1.0), MnS dissolution occurred as the first step, and the second step was the initiation of intergranular corrosion. Finally, dissolution of the steel matrix occurred. The role of MnS in the initiation of intergranular corrosion and depassivation of sensitized steel is discussed.

INTRODUCTION

In stainless steels, sulfide inclusions such as MnS act as initiation sites for pitting corrosion and have been the focus of many studies[1–7]. However, limited research has been conducted on the role of sulfide inclusions in the intergranular corrosion and depassivation of sensitized stainless steels[8].

Cr depletion owing to the formation of Cr-carbides at the grain boundaries is known to decrease the corrosion resistance of stainless steels. When stainless steels are heated to ~1000 K, such as by welding, Cr-carbides precipitate at the grain boundaries, causing Cr depletion[9]. Cr depletion occurs not only along grain boundaries but also at phase boundaries (γ/α, σ/α)[10,11], oxide inclusions[12], and Cr-nitrides[13,14]. Moreover, in ferritic stainless steels, spinodal decomposition causes Cr depletion[15,16]. Because the processes of heating and cooling are repeated in additive manufacturing, the occurrence of Cr depletion should be noted[17,18]. Thus, Cr depletion is an important factor to consider when analyzing the causes of corrosion in heat-treated stainless steels. The degree of sensitization (Cr depletion) has been successfully assessed based on the weight loss and/or inter-granular corrosion morphology in acids with a pH lower than the depassivation pH, such as via the Huey, Strauss, and Streicher tests[19]. Although the depassivation of Cr-depleted regions and intergranular corrosion occur in acidic solutions, stainless steels are regularly used in solutions with pH values higher than the depassivation pH. Therefore, in this study, the corrosion behavior of a sensitized stainless steel was investigated in a near-neutral pH and acidic solutions.

In chloride solutions at near-neutral pH, corrosion occurs with pitting morphology even in sensitized stainless steels, and thus, the corrosion resistance is assessed by the pitting potential. For example, Ziętala et al.[20] studied the corrosion resistance of Type 316 L stainless steel fabricated using laser-engineered net shaping (LENS). They reported that the lower pitting corrosion resistance of the LENS-fabricated 316 L was due to the formation of Cr-depleted regions in the steel matrix. Ganesh et al.[21] studied the corrosion and sensitization of laser rapidly manufactured (LRMed) Type 316 L stainless steel. With respect to the wrought specimens, the LRMed steel exhibited a lower pitting corrosion resistance. The pitting potential of stainless steels decreases with decreasing Cr

concentration[22]. Therefore, the lower pitting corrosion resistance of stainless steels produced via heat treatment is attributed to Cr depletion; however, there are other factors that lower pitting corrosion resistance, such as sulfide inclusions[1–7].

In the case of depassivation, the corrosion resistance of stainless steels also decreases with decreasing Cr concentration[23,24]. Therefore, the ready occurrence of the depassivation of sensitized steels can be explained by Cr depletion. However, sulfide inclusions should be considered in this explanation because dissolution species of sulfide have been reported to promote depassivation[6]. The existence of sulfide inclusions in Cr-depleted regions is expected to initiate the depassivation process, but to the best of our knowledge, the details have not been reported. Sulfide inclusions are crucial factors in the initiation of pitting in stainless steels[25–30]. Chiba et al. [6] reported that a small area without MnS exhibited an extremely high pitting potential exceeding 0.6 V (vs. Ag/AgCl, 3.33 M KCl), even for Type 304 stainless steel in 3 M NaCl at 298 K. In a small area where MnS was absent, Takayama et al. [31]. demonstrated that no pitting was generated on Type 304 stainless steel, even when potentio-dynamic polarization was performed up to the oxygen evolution region in 1 M NaCl at 348 K. Furthermore, it was reported that the depassivation of solution-treated Type 304 stainless steel in acidic NaCl solutions was initiated by localized dissolution, such as pitting corrosion, rather than general corrosion[25]. Therefore, sulfide inclusion dissolution is expected to be involved in the depassivation of stainless steels.

In this study, the role of MnS in the initiation of intergranular corrosion and depassivation of sensitized stainless steel was studied in 1 M NaCl at pH 5.4 and 1.0. The relationship between pitting at MnS and intergranular corrosion was investigated at pH 5.4. The relationships among MnS dissolution, intergranular corrosion, and depassivation were investigated at pH 1.0. Real-time in situ observations were performed on a small area of MnS. A re-sulfurized Type 304 stainless steel was used because large MnS inclusions are suitable for observing inclusion dissolution. The technique of fabricating a small electrode area containing a single corrosion initiation site and observing the surface during electrochemical measurements is simple but effective for elucidat-ing localized corrosion mechanisms[32–37].

[1]Department of Materials Science, Graduate School of Engineering, Tohoku University, 6-6-02, Aza-Aoba, Aramaki, Aoba-ku, Sendai 980-8579, Japan. [2]Present address: Central Research Institute of Electric Power Industry, 2-6-1, Nagasaka, Yokosuka 240-0196, Japan. ✉email: masashi.nishimoto.b8@tohoku.ac.jp; mutoi@material.tohoku.ac.jp
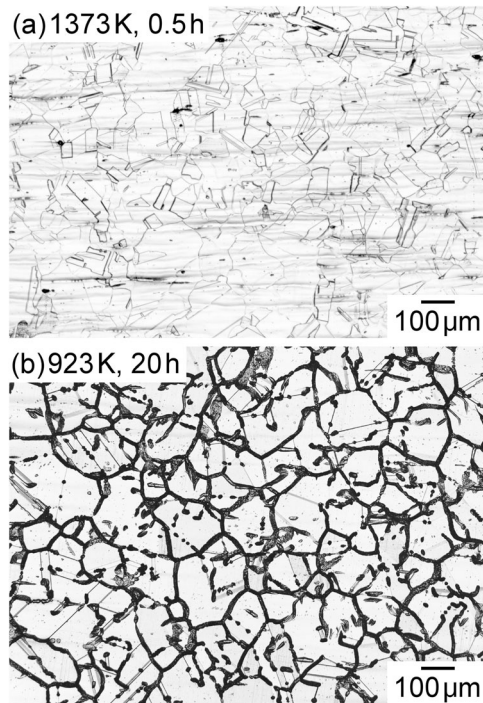
Fig. 1 OM images of re-sulfurized Type 304 stainless steel after electrolytic etching. a Solution-treated specimen and **b** sensitized specimen. Electrolytic etching was conducted in 10 mass% oxalic acid at a current density of 1×10^4 A m^{-2} for 90 s.

RESULTS

Material characterization

Figure 1 shows optical microscopy (OM) images of the solution-treated and sensitized specimens after electrolytic etching in 10 mass% oxalic acid. The grain boundaries of the solution-treated specimen were slightly etched, but almost all of the grain boundaries of the sensitized specimen were heavily etched, indicating that the steel was fully sensitized by heat treatment at 923 K for 20 h[38].

Figure 2a shows a scanning transmission electron microscopy (STEM) image of a grain boundary of the sensitized specimen. For this observation, a focused ion beam (FIB) lift-out specimen was prepared along Line 1 to traverse the grain boundary, as shown in the inset of Fig. 2a. Figure 2b shows the EDS map of Cr in the area surrounded by yellow lines in Fig. 2a, and Fig. 2c shows the results of the energy-dispersive X-ray spectroscopy (EDS) line analysis of the Cr concentration along Line A–B shown in Fig. 2a, b. In the STEM image, precipitates were observed along the grain boundary, and Cr accumulated in the precipitates, as seen in Fig. 2b, c. The electron diffraction patterns of the precipitates were consistent with those of $Cr_{23}C_6$ (figure not shown). In Fig. 2b, c, Cr was clearly depleted near the grain boundary precipitates, and the minimum Cr concentration was ~8 mass%. The above results indicate that Cr depletion occurred at the grain boundaries of the sensitized specimen.

Figure 3a shows an OM image of the as-polished surface of the sensitized specimen. In the steel used in this study, S was added to form MnS inclusions, and large elongated inclusions were observed. Figure 3b shows a scanning electron microscopy (SEM) image of a typical inclusion and the corresponding EDS maps. Mn and S were clearly detected in the inclusion. The intensity of the Cr signal in the inclusion was weaker than that in the steel matrix. However, a small amount of Cr was detected in the inclusion. The relative concentrations at Point 1 were Fe: 15 at.%, Cr: 9 at.%, Ni: 2 at.%, Mn: 37 at.%, and S: 37 at.%. In
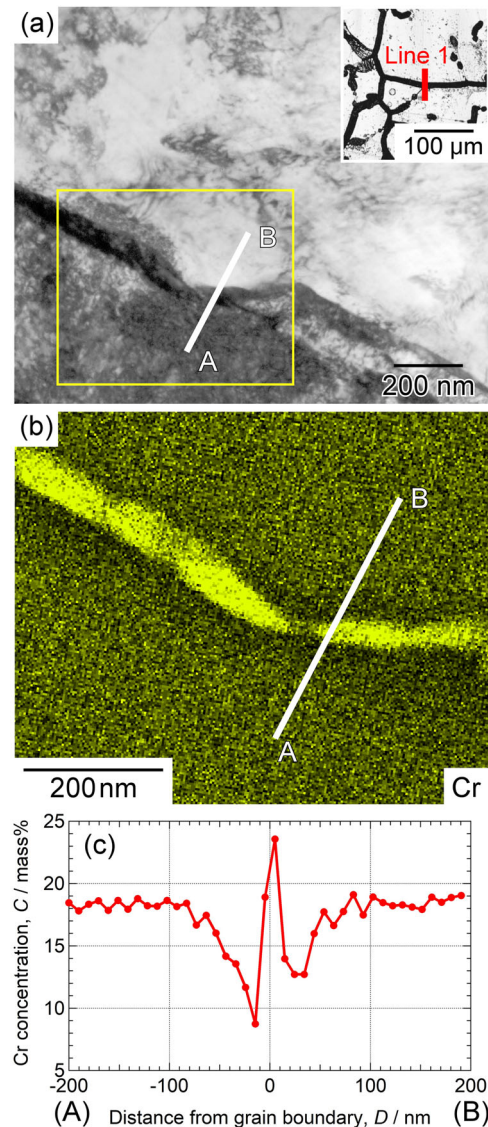

Fig. 2 Precipitates and Cr concentration at a grain boundary of sensitized re-sulfurized Type 304 stainless steel. a STEM image of a cross-section of the sensitized grain boundary shown in the inset. **b** EDS map of Cr in the area surrounded by yellow lines in **a**. **c** Cr concentration along the line from A to B in **a** and **b**.

addition to Cr, Fe was detected. Some of Cr and Fe signals may have originated from the steel matrix, but the inclusion was hypothesized to be MnS with small amounts of Cr and Fe, e.g., (Mn, Cr, Fe)S, because the existence of this type of inclusion has been reported in a duplex stainless steel[39]. For simplicity, this type of inclusion is referred to as MnS herein. No differences in the composition and morphology of the MnS inclusions were observed between the solution-treated and sensitized specimens. Furthermore, there were no differences between the MnS inclusions on the grain boundaries and those in the grains in terms of composition and morphology.

Pitting corrosion resistance

Figure 4a shows the potentiodynamic polarization curves of the solution-treated and sensitized specimens in 1 M NaCl (pH 5.4). For these measurements, the electrode area was 1 cm × 1 cm. For both specimens, potentiodynamic polarization was started at −0.2 V, and the cathodic current was measured until ~−0.1 V;

then, the anodic current was measured. Above −0.03 V, small current oscillations due to metastable pitting were generated for both specimens. As shown in Fig. 4a, sensitization lowered the pitting potential. Figure 4b, c shows SEM images of a corroded area and the corresponding EDS maps of S and Mn. For the solution-treated specimen, pits with lacy covers, which were thought to be generated at the MnS inclusions, were generated. In the sensitized specimen, pits with streaks similar to intergranular corrosion were observed. The corrosion was also thought to be initiated at MnS inclusions because S and Mn signals were detected near the corroded areas. Because the streaks were generated only for the sensitized specimen, they were attributed to intergranular corrosion due to Cr depletion.
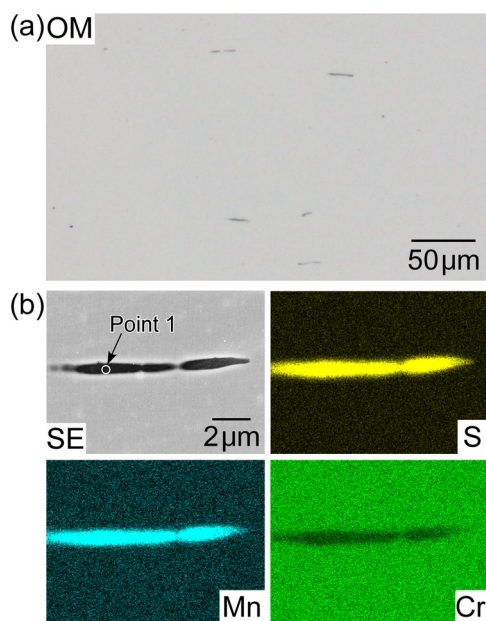

Fig. 3 Inclusions in sensitized re-sulfurized Type 304 stainless steel. a OM image of an as-polished surface. **b** SEM image of an inclusion and the corresponding EDS maps.

Correlation of pitting at MnS and intergranular corrosion

On the sensitized specimen, a small area with MnS at a grain boundary was fabricated (electrode area: ~100 μm × 100 μm), and potentiodynamic polarization was performed in 1 M NaCl (pH 5.4). In this study, the corrosion morphology was classified into three types: Specimens I–III. Figure 5a shows the micro-scale anodic polarization curves of Specimens I–III, and Fig. 5b–j shows the electrode surfaces of these specimens. Figure 5b–d shows composite images of the MnS inclusions and sensitized grain boundaries before preparation of the electrode areas. The black-and-white images of the MnS inclusions on the as-polished surfaces were inverted and superimposed on the OM images after electrolytic etching. These composite images indicate that MnS was located at the sensitized grain boundaries. Figure 5e–j shows the electrode areas before and after polarization, respectively. One or two MnS inclusions with a length of ~20 μm were included in the electrode area, and corrosion occurred at the inclusions.

As shown in Fig. 5a, above 0.1 V, the anodic current gradually increased with the electrode potential. Unlike the macro-scale polarization (electrode area: 1 cm × 1 cm) shown in Fig. 4a, the number of current oscillations decreased considerably, and the potential region where the oscillations occurred increased to higher than 0.25 V. Moreover, a further increase in current was observed in the potential range of 0.25–0.4 V. This increase in current was attributed to the anodic dissolution of MnS inclusions[6,33,40–43]. Many dissolution mechanisms have been proposed for MnS[1–5]. As one of them, Lott and Alkire[4] proposed the following series of reactions during anodic polarization of MnS.

$$2MnS + 3H_2O \rightarrow 2Mn^{2+} + S_2O_3{}^{2-} + 8H^+ + 8e^- \tag{1}$$

$$MnS + 2H^+ \rightarrow Mn^{2+} + S + H_2 \tag{2}$$
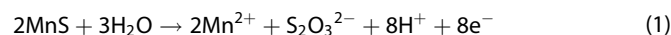
In this MnS dissolution potential range, trenching is known to occur at the MnS/steel boundaries, and pits are reported to be initiated in the trenches[6,31,43]. For Specimens I and II, a large current increase was observed around 0.35 V, suggesting the initiation of pitting corrosion. After anodic polarization, localized corrosion was confirmed at MnS, as shown in Fig. 5h, i. In Specimen III, current oscillations were observed three times ~0.35 V. However, no further large increase in current indicative of stable pitting was observed. At ~0.4 V, the anodic current decreased. As shown in Fig. 5j, the extent of corrosion damage
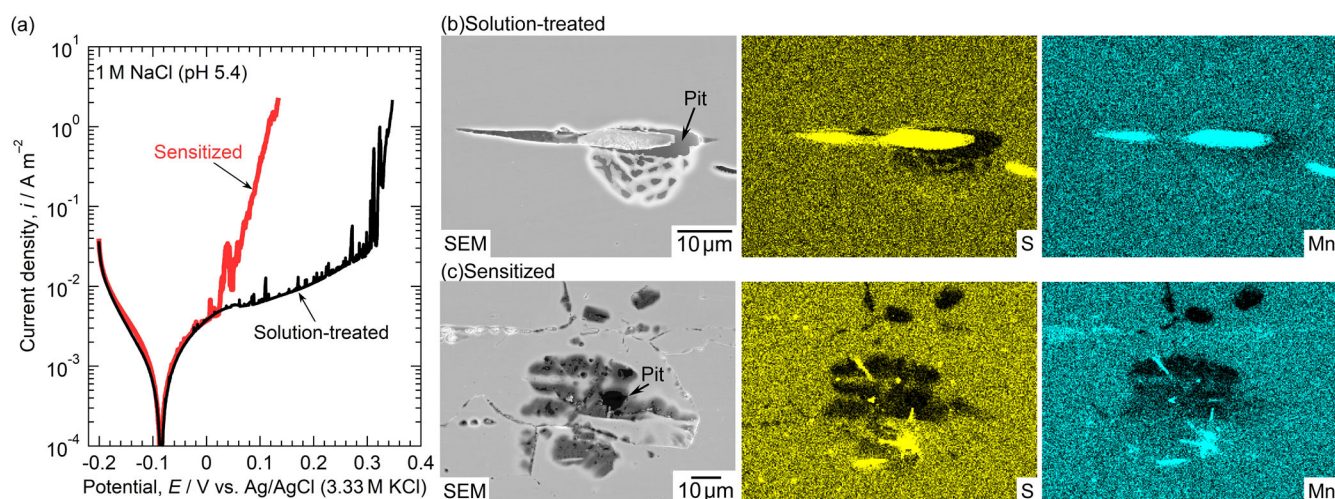

Fig. 4 Pitting potentials and corrosion morphology of solution-treated and sensitized re-sulfurized Type 304 stainless steel in naturally aerated 1 M NaCl (pH 5.4). a Potentiodynamic anodic polarization curves (electrode area: 1 cm × 1 cm). **b, c** SEM images of localized corrosion initiated on the **b** solution-treated specimen and **c** sensitized specimen.
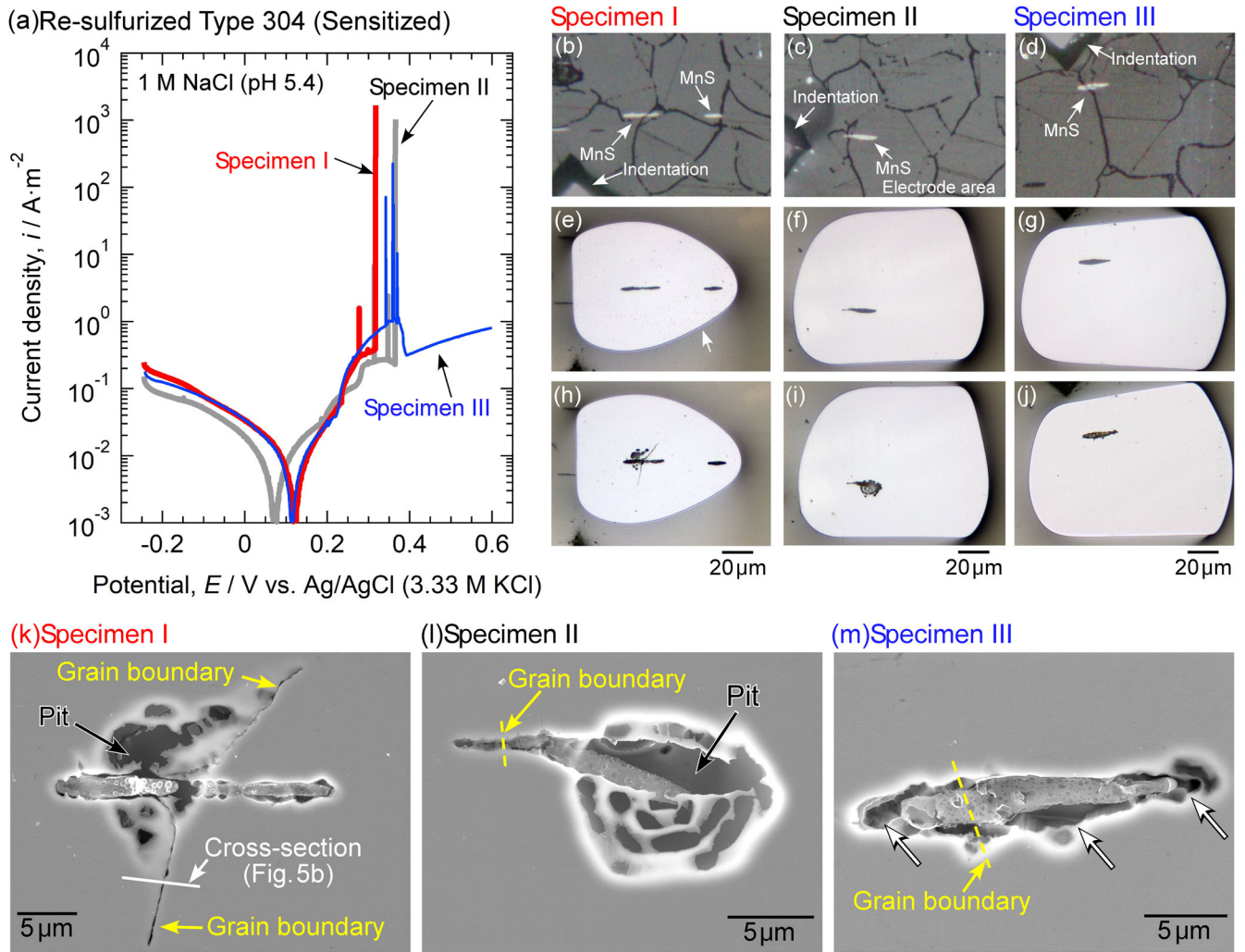
Fig. 5 Relationship between polarization behavior and corrosion morphology at MnS on the sensitized re-sulfurized Type 304 stainless steel. a Micro-scale anodic polarization curve of a small area with MnS at a sensitized grain boundary in naturally aerated 1 M NaCl. **b–d** Composite OM images of MnS inclusions and sensitized grain boundaries. **e–g, h–j** OM images of electrode areas **e–g** before and **h–j** after anodic polarization. **k–m** SEM images of localized corrosion: **k** Specimen I, **l** Specimen II, and **m** Specimen III.

around the MnS inclusions was relatively low compared to Specimens I and II.

Figure 5k shows an SEM image of the corrosion on Specimen I. In this image, a pit initiated at the MnS inclusion. Moreover, streaks resembling intergranular corrosion were observed on the upper and lower sides of the inclusion. The positions of these streaks were consistent with those of the sensitized grain boundaries (Fig. 5b). Therefore, these streaks were concluded to be intergranular corrosion owing to the dissolution of Cr-depleted regions. In Specimen II (Fig. 5l), only one pit was observed at the MnS inclusion. In this case, no intergranular corrosion was initiated. In Specimen III, only the dissolution of the MnS/steel boundary was observed. There are several mechanisms as to the reason for trench formation[6,42,44,45], but we believe that the synergistic effect of chloride ions and elemental sulfur generated from MnS causes depassivation of the steel matrix around MnS and the formation of trenches[6]. The positions indicated by the white arrows in Fig. 5m were relatively heavily corroded. These were thought to correspond to metastable pits; however, these pits were not located at the grain boundary. In the pitting corrosion at MnS inclusions, it has been demonstrated that a trench is first formed at the MnS/steel boundary, and pits are subsequently generated inside the trench[6,31,43]. In this study, no

intergranular corrosion was found to occur from the trench, even when MnS was present in Cr-depleted regions.

In situ OM images of the electrode area of Specimen I are shown in Fig. 6a–m. These images were obtained from the video recording during anodic polarization shown in Fig. 5a. Figure 6a presents the surface at the open-circuit potential (OCP) before polarization. After the start of polarization until the potential reached 0.19 V, almost no change in color was observed at the inclusion, as shown in Fig. 6b. Above ~0.25 V, a part of the MnS inclusion turned white, as indicated by the arrow shown in Fig. 6c. This whitening may indicate dissolution of MnS. Figure 6d shows the image taken immediately before the initiation of pitting; the time of this image was defined as 0 s. The current density at this time was 0.61 A m^{-2}. In Fig. 6d–g, the inset images are enlarged views of the areas surrounded by white lines in each figure. The yellow dashed lines in the insets are drawn at the same position as the guide to the MnS/steel boundary. At 0.16 s, the current density increased to 5.0 A m^{-2}. However, no changes were observed in or around the inclusion. HhAt 0.5 s, the current density further increased by approximately one order of magnitude to 90 A m^{-2}, and a small dark area appeared at the MnS/steel boundary, as indicated by the black thick arrow in Fig. 6f. This area was thought to be the mouth of the stable pit, based on a comparison of this
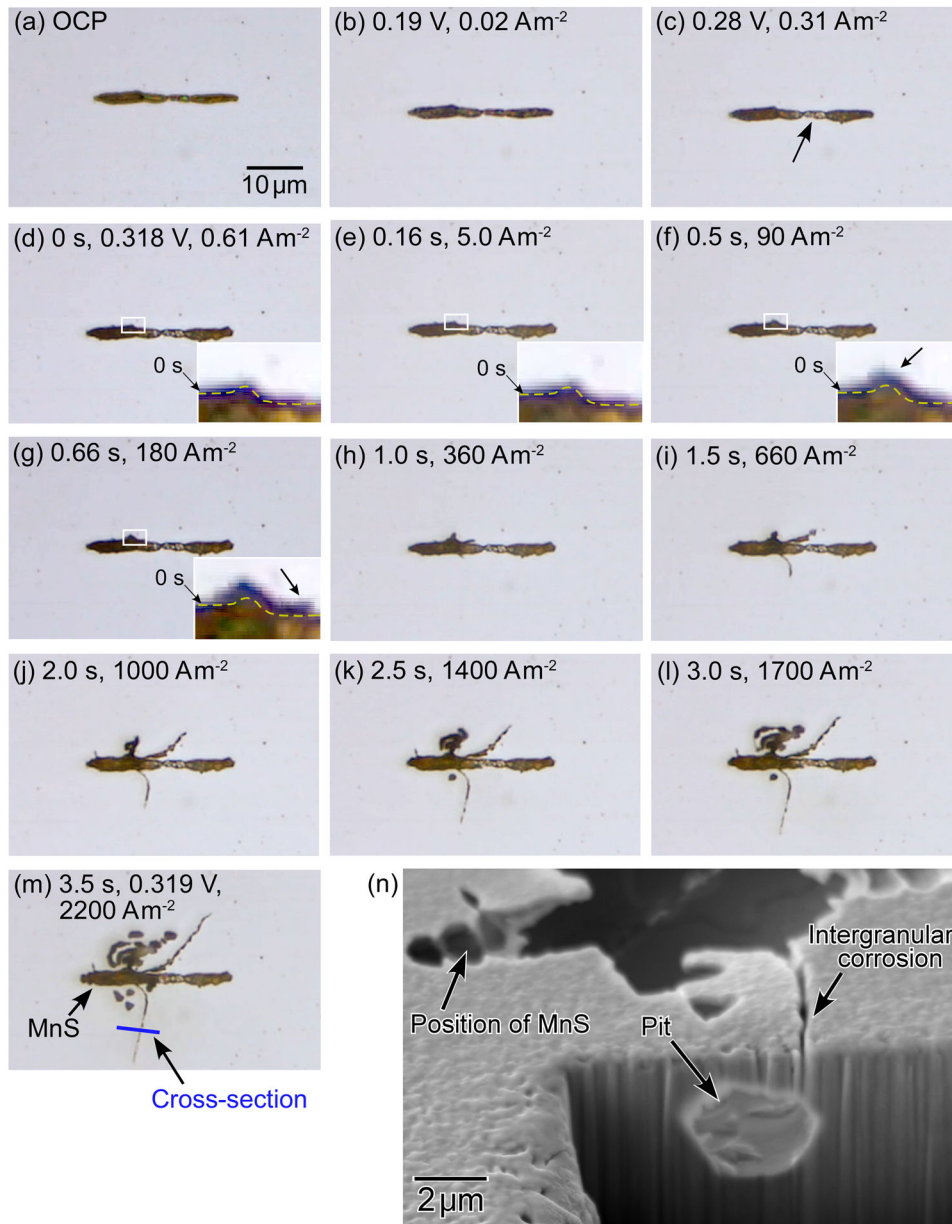
Fig. 6 Initiation behavior of pitting and intergranular corrosion on the sensitized re-sulfurized Type 304 stainless steel. a–m In situ images of the initiation of pitting and intergranular corrosion on Specimen I during the anodic polarization shown in Fig. 5a. **n** SEM image of the cross-section on Specimen I shown in Figs. 5k and 6m.

image and Fig. 5k. At 0.66 s, as seen in the inset of Fig. 6g, the dark area extended to the right along the MnS/steel boundary. This suggests that the pit expanded to the right. After 1.0 s, intergranular corrosion was initiated and grew with time, as shown in Fig. 6h–m.

Figure 6n shows an SEM image of the cross-section of Specimen I. The location of the cross-section is shown in Figs. 5k and 6m. MnS dropped out during fabrication of the cross-section. Moreover, a cavity (pit) appeared under the MnS. A part of the pit appeared in the cross-section as a hole, indicating that the pit was in contact with the Cr-depleted region. The hole appeared to be far from the initiation site of pitting, but this was likely due to the dissolution of the steel matrix beneath the inclusion and the wide spreading of the stable pit[37]. Based on the results thus far, it is considered that pitting corrosion initially occurred at MnS, and then intergranular corrosion was initiated when the corrosion reached a Cr-depleted region along the sensitized grain boundary.

Depassivation of the sensitized and solution-treated specimens

Figure 7a shows the change in OCP with decreasing pH for the sensitized and solution-treated specimens in 1 M NaCl. The initial pH of the solution was 5.4, and the pH was decreased stepwise using HCl. The large drop in the OCP to ~−0.4 V was due to depassivation, and the depassivation pHs of the sensitized and solution-treated specimens were 2 and 1, respectively. After the measurements, discoloration was observed around the MnS inclusions in both specimens as shown in Fig. 7b, c. The depassivation pH of the sensitized specimen was higher than that of the solution-treated specimen. This may be due to Cr depletion along the sensitized grain boundaries; however, MnS is likely to affect depassivation because discoloration was observed around the MnS inclusions.

To ascertain the effect of MnS on the depassivation at sensitized grain boundaries, a small area without MnS was fabricated on the
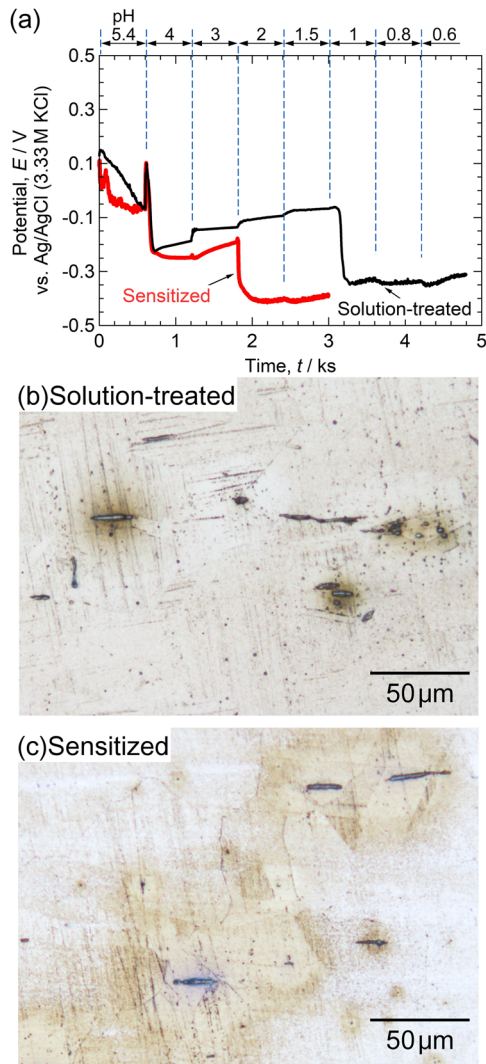
Fig. 7 Depassivation behavior of solution-treated and sensitized re-sulfurized Type 304 stainless steel. a Effect of pH on the OCPs of the solution-treated and sensitized specimens in 1 M NaCl (the pH was lowered stepwise with HCl). **b**, **c** OM images of the specimens after the OCP measurements in **a**: **b** solution-treated and **c** sensitized specimens.

Fig. 8 Corrosion resistance to depassivation of a small area containing the sensitized grain boundary without MnS inclusion. a Time variation of the OCP of a small area without MnS in the sensitized re-sulfurized Type 304 stainless steel in 1 M NaCl at pH 1.0. **b**, **c** OM images of the electrode area before and after the OCP measurements shown in **a**: **b** before, and **c** after measurement. **d**, **e** OM images of the electrode area after electrolytic etching: **d** 12 s and **e** 90 s.

sensitized specimen, and OCP measurements were performed in 1 M NaCl at pH 1.0. Figure 8a shows the time variation of the OCP, and Fig. 8b, c shows the electrode areas before and after the measurements, respectively. As seen in Fig. 8b, c, no MnS inclusions were present in the electrode area, and no corrosion was generated after the measurements. The pH of this solution was sufficiently low to observe depassivation because the depassivation pH of the sensitized specimen was determined to be 2, as shown in Fig. 7a. However, no large drop in the OCP to around −0.4 V was observed, indicating that no depassivation occurred. After the OCP measurements, the masking around the electrode area was stripped, and electrolytic etching was performed in 10 mass% oxalic acid at 1×10^4 A m^{-2}. Figure 8d, e shows the surface appearance of the electrode area after etching for 12 s and 90 s, respectively. Sensitized grain boundaries (Cr-depleted regions) were observed. Thus, it was expected that MnS was responsible for the depassivation of the sensitized specimen.

To analyze the effect of MnS inclusions on the depassivation of sensitized re-sulfurized Type 304 stainless steel, a small area with
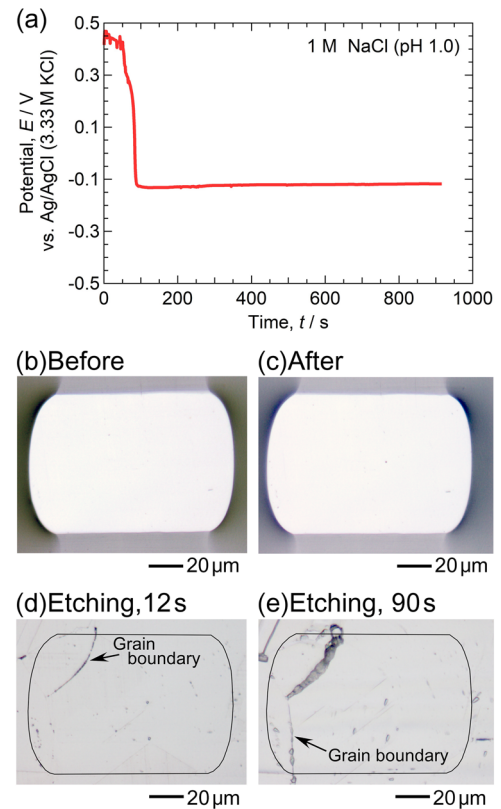
MnS at a sensitized grain boundary was immersed in 1 M NaCl at pH 1.0. Figure 9a shows the temporal variation of the OCP during immersion. Immediately after immersion, the OCP was ~0.21 V and became ~0.1 V from 7 to 13 s. At 14 s, the OCP further decreased and then stabilized at −0.4 V. Figure 9b shows an SEM image of the electrode area after immersion. Figure 9c shows an SEM image of the area surrounded by the yellow lines in Fig. 9b and the corresponding EDS maps of Mn and S. As shown in Fig. 9b, a grain boundary was present from the upper right to the lower left of the inclusion. In addition, Mn and S signals were not detected (Fig. 9c). Thus, an MnS inclusion located at the sensitized grain boundary was present in the electrode area, and MnS completely dissolved during immersion.

Figure 9d–o shows in situ observation images of the electrode area. Enlarged images of the area surrounded by the dashed lines shown in Fig. 9d–i are given in Fig. 9p–u. Figure 9d shows the surface immediately after immersion, which is defined as 0 s. At 17 s, a color change was observed in the MnS inclusion, implying that the surface of the MnS inclusion began to dissolve. In contrast, the grain boundaries and steel matrix did not dissolve during the initial stage of immersion because no color change was observed (Fig. 9e, q). After 18 s, a black streak appeared around the MnS inclusion at the position indicated by the black arrow in Fig. 9r. Because the location of the black streak corresponded to the grain boundary, it was determined to be intergranular corrosion owing to the dissolution of the Cr-depleted region. From 18 s to 21 s, the black streak lengthened, and another black streak was generated at the position indicated by the red arrow in
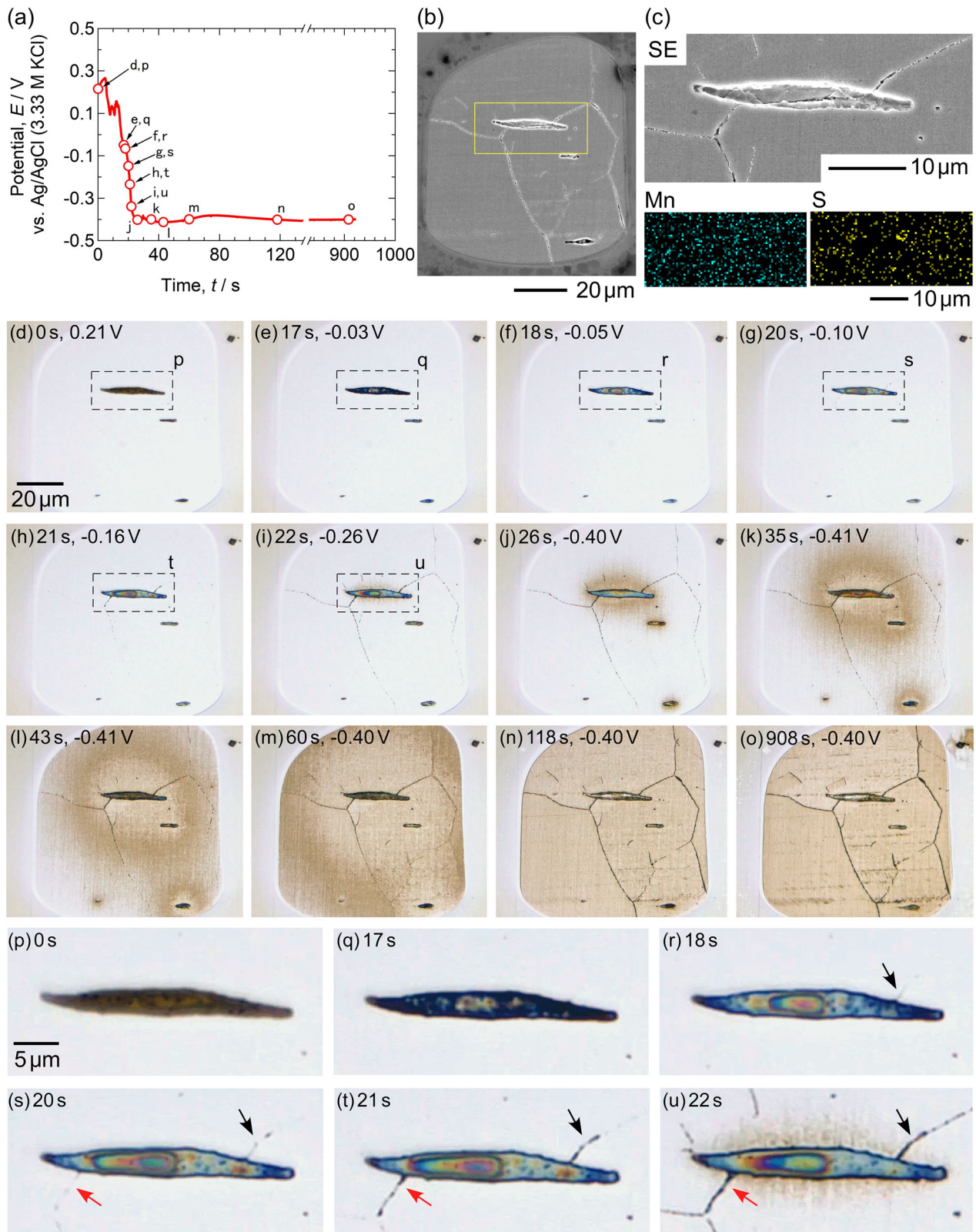
Fig. 9 Depassivation behavior at MnS on sensitized re-sulfurized Type 304 stainless steel. a Time variation of OCP in a small area with MnS at sensitized grain boundaries in 1 M NaCl at pH 1.0. **b** SEM image of the electrode area after immersion. **c** SEM image of the area surrounded by yellow lines in **b** and the corresponding EDS maps of Mn and S. **d**–**o** In situ observation images of the electrode area during immersion shown in **a**. **p**–**u** Enlarged OM images of the area surrounded by dashed lines in **d**–**i**.

Fig. 9s. At 22 s, the color of the steel matrix around the MnS inclusion began to change to brown, suggesting the beginning of the dissolution of the steel matrix. Subsequently, the discoloration around the inclusion expanded over time and spread to the entire electrode surface, as shown in Fig. 9j–o. This discoloration was attributed to the dissolution of the steel matrix. The in situ observations suggested that the MnS inclusion dissolved as the first step in the depassivation of the sensitized specimen. The second step was the dissolution of the Cr-depleted regions (i.e., the sensitized grain boundaries). Finally, dissolution of the steel matrix was determined to occur from the MnS and spread concentrically over the entire electrode surface.

Comparing Fig. 9a, d–o reveals that when the MnS inclusion began to dissolve, the OCP changed from 0.21 to −0.03 V (Fig. 9d, e). Then, from 18 to 21 s, dissolution of the grain boundaries occurred, and the OCP decreased to −0.16 V (Fig. 9f–h). After 22 s, the steel matrix began to corrode, and the OCP further decreased to −0.4 V (Fig. 9j). The OCP value of approximately −0.4 V was determined to be the onset of corrosion of the steel matrix. Comparison of the potential signal and corrosion behavior of the electrode surface reveals that the discoloration originating from the MnS inclusion was depassivation.

DISCUSSION

In the micro-scale polarization of the sensitized specimen shown in Fig. 5, the corrosion morphology at MnS was classified into three types: (1) pitting with intergranular corrosion (Specimen I), (2) pitting without intergranular corrosion (Specimen II), and (3) trenching without intergranular corrosion (Specimen III). First, we considered the causes of these three appearances. As shown in Fig. 6 (Specimen I), pitting corrosion initially occurred at MnS during potentiodynamic polarization in 1 M NaCl (pH 5.4), and then intergranular corrosion was thought to be generated when the pit reached a Cr-depleted region. Acidification generally occurs inside pits[46–50]. Therefore, the intergranular corrosion of Specimen I is thought to have been introduced through the depassivation of Cr-depleted regions by an acidic solution inside the pit. Even if pitting corrosion was generated at MnS, it was concluded that pitting corrosion did not result in intergranular corrosion when the pit location was distant from the sensitized grain boundaries, as in Specimen II. Moreover, even when MnS at a sensitized grain boundary dissolved and trenching occurred around the MnS, similar to Specimen III, no intergranular corrosion was generated from the trench. These results indicate that severe acidification, such as inside the pits, is essential to dissolve the Cr-depleted regions. Ida et al. [25]. demonstrated that the depassivation pH of a sensitized Type 304 stainless steel (S: 0.0026 mass%) was approximately 1. Thus, the pH of the solution in the pit causing intergranular corrosion is thought to be less than 1, whereas the solution in the trench around MnS is expected to be above pH 1.

Based on the above mechanism and the results shown in Figs. 5 and 6, at near-neutral pH, no intergranular corrosion is expected to occur directly from the Cr-depleted regions without MnS. In fact, it has been reported that neither pitting nor intergranular corrosion occurred at a single sensitized grain boundary without MnS in Type 304 stainless steel in 0.1 M NaCl (pH 5.4)[25]. This indicates that sensitization does not lower the corrosion resistance of stainless steels in NaCl solutions at near-neutral pH. However, as shown in Fig. 4a, the pitting potential decreases after sensitization. This can be explained by the possible overlap of MnS and Cr-depleted regions as follows. In stainless steels, MnS inclusions are randomly dispersed. The probability of pitting corrosion generated at the intersection of a sensitized grain boundary and an MnS inclusion is thus low; however, such a situation is thought to exist in macro-scale electrodes of sizes such as 1 cm × 1 cm. When a metastable pit occurs at MnS in Cr-depleted regions, the

metastable pit is likely to readily become a stable pit because of the low Cr concentration and the difficulty of repassivation. MnS inclusions have various shapes; the part of MnS responsible for pitting corrosion depends on its morphology, particularly its extent in the depth direction[51]. The overlap between the Cr-depleted region and the deep part of MnS is thought to decrease the critical potential for the transformation from metastable to stable pitting, resulting in a decrease in the pitting potential. It can be concluded that the pitting corrosion resistance of sensitized stainless steels is not determined by the existence of Cr depletion alone, but by the existence of MnS in the Cr-depleted regions.

Next, we discuss the results of the micro-scale experiments on the roles of MnS and Cr depletion in depassivation of sensitized steel. As shown in Fig. 9, MnS dissolution occurred as the first step in the depassivation of the sensitized specimen in 1 M NaCl at pH 1.0. The second step was dissolution of the sensitized grain boundary. Finally, corrosion (dissolution) of the steel matrix occurred. Moreover, even for the sensitized specimen, neither intergranular corrosion nor depassivation occurred in 1 M NaCl at pH 1.0 on the electrode area without MnS (Fig. 8). In other words, we can speculate that the dissolution of MnS must occur for intergranular corrosion and depassivation.

Chiba et al. demonstrated that elemental sulfur is deposited on and around MnS inclusions via MnS dissolution[6]. They also reported that active dissolution of Type 304 stainless steel occurred in solutions containing both elemental sulfur and chloride ions, even at pH 3.5. Sulfur deposition on steel surfaces is likely to accelerate depassivation[6]. Additionally, H_2S, HSO_3^-, and $S_2O_3^{2-}$ may be formed through MnS dissolution[1–6], and these species are also thought to contribute to the depassivation of stainless steels. The dissolution species of MnS are expected to lead to the dissolution of Cr-depleted regions, resulting in intergranular corrosion. Under open-circuit conditions in 1 M NaCl at pH 1, unlike the anodic polarization in 1 M NaCl (pH 5.4), H_2S released from MnS may be deeply involved in the depassivation because of its low potential[52,53].

Regarding the corrosion with discoloration spreading over the entire electrode surface in the final stage of Fig. 9, it is likely that MnS dissolution species are involved in depassivation of the steel matrix because the discoloration expands in a circular pattern centered on the inclusion. Therefore, it can be concluded that the dissolved species of MnS first cause depassivation of the grain boundaries with low Cr concentrations (Cr-depleted regions), and then cause depassivation of the intragranular regions with high Cr concentrations. As seen in Fig. 5m, during potentiodynamic polarization in 1 M NaCl at pH 5.4, intergranular corrosion (depassivation of the sensitized grain boundary) was not caused by MnS dissolution alone. This appears to be due to the high pH of the solution. As shown in Fig. 7a, depassivation of the sensitized specimen occurred at pH 2; therefore, acidification around pH 2 is thought to be required for depassivation of the Cr-depleted regions by the dissolution species of MnS.

In the macro-scale experiments shown in Fig. 7a, depassivation occurred on the solution-treated specimens even at pH 1. This may be because a larger electrode surface increases the probability of the existence of larger and deeper MnS inclusions, where the concentration of dissolved species is likely to be higher. At these points, depassivation may occur even on the solution-treated specimens.

In this work, the intergranular corrosion and depassivation of sensitized re-sulfurized Type 304 stainless steel were studied in 1 M NaCl at pH 5.4 and 1.0, respectively. The following conclusions were drawn:

1. During potentiodynamic polarization in 1 M NaCl (pH 5.4), intergranular corrosion of the sensitized Type 304 stainless steel occurred after pit initiation at an MnS inclusion. Intergranular corrosion was determined to occur when the pitting corrosion

Table 1. Chemical composition of stainless steel (mass%).

C	Si	Mn	P	S	Ni	Cr
0.051	0.39	1.51	0.039	0.0215	8.27	18.3
Mo	Cu	Al	N	O	Fe	
0.21	0.35	0.002	0.0799	0.0023	Balance	

reached a Cr-depleted region along the sensitized grain boundaries.

2. The pitting corrosion resistance of the sensitized Type 304 stainless steel was not determined by the existence of Cr depletion alone but by the existence of MnS in the Cr-depleted regions.

3. In the depassivation of sensitized re-sulfurized Type 304 stainless steel in 1 M NaCl at pH 1.0 under open-circuit conditions, the dissolution of MnS inclusions occurred as the first step. The second step was intergranular corrosion owing to the dissolution of Cr-depleted regions. Finally, depassivation of the intragranular regions occurred.

4. Even on the sensitized specimen, neither intergranular corrosion nor depassivation occurred in 1 M NaCl at pH 1.0 on the small electrode area without MnS. The dissolved species of MnS were determined to cause depassivation of the sensitized grain boundaries and intragranular regions.

METHODS
Specimens and electrolytes
A re-sulfurized Type 304 stainless steel was used as the specimen; the chemical composition is listed in Table 1. The concentration of S was 0.0215 mass%, which is close to the upper limit for Type 304 stainless steel (0.030 mass%). For the solution treatment, the steel was heat-treated at 1373 K for 0.5 h and quenched in water. After solution treatment, the steel was sensitized by heating at 923 K for 20 h and quenching in water. For the steel used in this study, not all grain boundaries were sensitized by the commonly used 2 h heat treatment; therefore, sensitization was performed for 20 h. After heat treatment, the steel was cut into small specimens (20 × 25 × 2 mm). Before the electrochemical measurements, the specimens were mechanically ground using SiC paper through 1500 grit, polished using a 1 μm diamond paste, and finally degreased with ethanol.

As electrolytes, 1 M NaCl (pH 5.4, unadjusted) and 1 M NaCl (pH 1.0, adjusted with HCl) were used for the electrochemical measurements. All solutions were prepared using deionized water and analytical-grade chemicals.

Electrochemical measurements
Potentiodynamic polarization was conducted in 1 M NaCl (pH 5.4, unadjusted). The scan rate was 23 mV min^{-1}. To ascertain the depassivation behavior, the time variation of the OCP was monitored in 1 M NaCl (pH 1.0, adjusted with HCl). In addition, the pH was lowered stepwise using HCl, and the depassivation pH in 1 M NaCl was determined from the change in the OCP. All electrochemical measurements were performed at 298 K under naturally aerated conditions, and the working electrode area was ~1 × 1 cm or 100 × 100 μm. For the former macro-scale measurements, the electrodes were sealed with epoxy resin and paraffin. In the latter micro-scale measurements, the electrode areas were fabricated using a coating method, and real-time in situ observations of the electrode area were performed using an optical microscope equipped with a water-immersion objective lens (×100 magnification). Details of the micro-electrochemical system used in this study can be found elsewhere[37]. The working electrode areas were precisely measured after polarization, and the current values were converted to current densities. All of the

potentials cited herein are expressed in terms of the Ag/AgCl (3.33 M KCl) electrode (0.206 V vs. the standard hydrogen electrode at 298 K).

In this study, a small area containing MnS located at a sensitized grain boundary was fabricated. To choose an MnS inclusion located at a sensitized grain boundary, electrolytic etching in 10 mass% oxalic acid was first conducted at a current density of 1×10^4 A m^{-2} for 20 s, and indentations were formed to mark the position of sensitized grain boundaries. The specimen surface was then polished again using diamond paste. Subsequently, one MnS inclusion located at a sensitized grain boundary was selected as the target, and the working electrode area was fabricated. Because the MnS inclusions were darker gray than the steel matrix, they were clearly visible in the as-polished condition without etching.

Microstructural characterization
Before and after the electrochemical measurements, the electrode areas were imaged using OM, and the corrosion morphology and elemental distribution at and around the corrosion initiation sites were analyzed using field-emission SEM coupled with EDS. The acceleration voltage for the SEM/EDS analysis was 20 kV. When necessary, cross-sections of the corrosion sites were fabricated using a FIB system: a targeted area was milled with a Ga ion beam.

STEM coupled with EDS was used to observe and analyze the sensitized grain boundaries. The accelerating voltage was 200 kV. The probe size was *ca*. 1 nm. The specimens for STEM observations were prepared using a FIB system and lifted out using a manipulator. Before the STEM specimen preparation, the steel surface was electrolytically etched in 10 mass% oxalic acid at 1×10^4 A m^{-2} for 90 s and indented to mark the positions of the etched grain boundaries. The steel surface was then polished, and the STEM specimen was obtained from the sensitized grain boundary.

REFERENCES
1. Eklund, G. S. Initiation of pitting at sulfide inclusions in stainless steel. *J. Electrochem. Soc.* **121**, 467–473 (1974).
2. Castle, J. E. & Ke, R. Studies by Auger spectroscopy of pit initiation at the site of inclusions in stainless steel. *Corros. Sci.* **30**, 409–428 (1990).
3. Wranglén, G. Pitting and sulphide inclusions in steel. *Corros. Sci.* **14**, 331–349 (1974).
4. Lott, S. E. & Alkire, R. C. The role of inclusions on initiation of crevice corrosion of stainless steel. *J. Electrochem. Soc.* **136**, 973–979 (1989).
5. Webb, E. G. & Alkire, R. C. Pit initiation at single sulfide inclusions in stainless steel. *J. Electrochem. Soc.* **149**, B280–B285 (2002).
6. Chiba, A., Muto, I., Sugawara, Y. & Hara, N. Pit initiation mechanism at MnS inclusions in stainless steel: synergistic effect of elemental sulfur and chloride ions. *J. Electrochem. Soc.* **160**, C511–C520 (2013).
7. Amatsuka, S. et al. Micro-electrochemical insights into pit initiation site on aged UNS S32750 super duplex stainless steel. *npj Mater. Degrad.* **7**, 15 (2023).
8. Altamirano, P. M., Kappes, M. A. & Rodríguez, M. A. Effect of some environmental and stainless steel metallurgical variables on the values of degree of sensitization measured by the double loop-electrochemical potentiokinetic reactivation test. *Corrosion* **78**, 1067–1078 (2022).
9. Srinivasan, N. Sensitization of austenitic stainless steels: current developments, trends, and future directions. *Metallogr. Microstruct. Anal.* **10**, 133–147 (2021).
10. Tarasov, S. Y. et al. Microstructural evolution and chemical corrosion of electron beam wire-feed additively manufactured AISI 304 stainless steel. *J. Alloys Compd.* **803**, 364–370 (2019).
11. Sathirachinda, N., Pettersson, R. & Pan, J. Depletion effects at phase boundaries in 2205 duplex stainless steel characterized with SKPFM and TEM/EDS. *Corros. Sci.* **51**, 1850–1860 (2009).

12. Wang, K. et al. On the pitting behaviour of laser powder bed fusion prepared 316L stainless steel upon post-processing heat treatments. *Corros. Sci.* **197**, 110060 (2022).

13. He, L., Wirian, L. & Singh, P. M. Effects of isothermal aging on the microstructure evolution and pitting corrosion resistance of lean duplex stainless steel UNS S32003. *Metall. Mater. Trans. A* **50**, 2103–2113 (2019).

14. Sun, J., Tang, H., Wang, C., Han, Z. & Li, S. Effects of alloying elements and microstructure on stainless steel corrosion: a review. *Steel Res. Int.* **93**, 2100450 (2022).

15. Silva, R. et al. A comprehensive study of the pitting corrosion mechanism of lean duplex stainless steel grade 2404 aged at 475 °C. *Corros. Sci.* **191**, 109738 (2021).

16. Silva, R. et al. New insights into the hardening and pitting corrosion mechanisms of thermally aged duplex stainless steel at 475 °C: A comparative study between 2205 and 2101 steels. *J. Mater. Sci. Technol.* **98**, 123–135 (2022).

17. Vukkum, V. B. & Gupta, R. K. Review on corrosion performance of laser powder-bed fusion printed 316L stainless steel: effect of processing parameters, manufacturing defects, post-processing, feedstock, and microstructure. *Mater. Des.* **221**, 110874 (2022).

18. Weng, F. et al. Enhanced corrosion resistance of laser aided additive manufactured CoCrNi medium entropy alloys with oxide inclusion. *Corros. Sci.* **195**, 109965 (2022).

19. Pettersson, C. O., Boellinghaus, T. & Kannengiesser, T. Corrosion testing of welds, a review of methods. *Weld World* **51**, 79–106 (2007).

20. Ziętala, M. et al. The microstructure, mechanical properties and corrosion resistance of 316 L stainless steel fabricated using laser engineered net shaping. *Mater. Sci. Eng. A* **677**, 1–10 (2016).

21. Ganesh, P. et al. Studies on pitting corrosion and sensitization in laser rapid manufactured specimens of type 316L stainless steel. *Mater. Des.* **39**, 509–521 (2012).

22. Charles, J., Mithieux, J.-D., Santacreu, P.-O. & Peguet, L. The ferritic stainless family: the appropriate answer to nickel volatility? *Rev. Met. Paris* **106**, 124–139 (2009).

23. Crolet, J. L., Séraphin, L. & Tricot, R. Influence des teneurs en chrome, molybdène et soufre sur la résistance à la corrosion caverneuse des aciers inoxydables. *Rev. Met. Paris* **72**, 937–948 (1975).

24. Mujanović, E. et al. Depassivation and repassivation of stainless steels by stepwise pH change. *Mater. Corros.* **72**, 421–433 (2021).

25. Ida, N., Muto, I., Sugawara, Y. & Hara, N. Local electrochemistry and in situ microscopy of pitting at sensitized grain boundary of type 304 stainless steel in NaCl solution. *J. Electrochem. Soc.* **164**, C779–C787 (2017).

26. Tokuda, S., Muto, I., Sugawara, Y. & Hara, N. The role of applied stress in the anodic dissolution of sulfide inclusions and pit initiation of stainless steels. *Corros. Sci.* **183**, 109312 (2021).

27. Tokuda, S., Muto, I., Sugawara, Y. & Hara, N. Effect of sensitization on pitting corrosion at MnS and CrS in type 304 stainless steel. *J. Electrochem. Soc.* **168**, 091504 (2021).

28. Liu, P., Zhang, Q.-H., Watanabe, Y., Shoji, T. & Cao, F.-H. A critical review of the recent advances in inclusion-triggered localized corrosion in steel. *npj Mater. Degrad.* **6**, 81 (2022).

29. Nishimoto, M., Muto, I. & Sugawara, Y. Review—understanding and controlling the electrochemical properties of sulfide inclusions for improving the pitting corrosion resistance of stainless steels. *Mater. Trans.* **64**, 2051–2058 (2023).

30. Sun, Y. et al. Mechanisms of inclusion-induced pitting of stainless steels: a review. *J. Mater. Sci. Technol.* **168**, 143–156 (2024).

31. Takayama, R., Nishimoto, M., Muto, I. & Sugawara, Y. Micro-electrochemical aspects of the effects of temperature on pit initiation at MnS Inclusion in type 304 stainless steel. *J. Electrochem. Soc.* **169**, 111501 (2022).

32. Nishimoto, M., Muto, I., Sugawara, Y. & Hara, N. Artificial MnS inclusions in stainless steel: fabrication by spark plasma sintering and corrosion evaluation by microelectrochemical measurements. *ISIJ Int.* **60**, 196–198 (2020).

33. Nishimoto, M., Muto, I., Sugawara, Y. & Hara, N. Passivity of (Mn,Cr)S inclusions in type 304 stainless steel: the role of Cr and the critical concentration for preventing inclusion dissolution in NaCl solution. *Corros. Sci.* **176**, 109060 (2020).

34. Shao, Z., Nishimoto, M., Muto, I. & Sugawara, Y. Real-time in situ observation of the corrosion process of die-cast AZ91D magnesium alloy in NaCl solutions under galvanostatic polarization. *Corros. Sci.* **192**, 109834 (2021).

35. Shao, Z., Nishimoto, M., Muto, I. & Sugawara, Y. Fabrication of a model specimen for understanding micro-galvanic corrosion at the boundary of α-Mg and β-Mg$_{17}$Al$_{12}$. *J. Magnes. Alloys* **11**, 137–153 (2023).

36. Kakinuma, H. et al. Change in oxygen reduction reactivity of intermetallics: a mechanism of the difference in trenching around Al–Fe and Al–Fe–Si particles on AA1050 in NaCl. *J. Electrochem. Soc.* **170**, 021503 (2023).

37. Chiba, A., Muto, I., Sugawara, Y. & Hara, N. A microelectrochemical system for in situ high-resolution optical microscopy: Morphological characteristics of pitting at MnS inclusion in stainless steel. *J. Electrochem. Soc.* **159**, C341–C350 (2012).

38. Lima, A. S., Nascimento, A. M., Abreu, H. F. G. & de Lima-Neto, P. Sensitization evaluation of the austenitic stainless steel AISI 304L, 316L, 321 and 347. *J. Mater. Sci.* **40**, 139–144 (2005).

39. Jeon, S.-H., Kim, S.-T., Lee, I.-S. & Park, Y.-S. Effects of sulfur addition on pitting corrosion and machinability behavior of super duplex stainless steel containing rare earth metals: part 2. *Corros. Sci.* **52**, 3537–3547 (2010).

40. Muto, I., Izumiyama, Y. & Hara, N. Microelectrochemical measurements of dissolution of MnS inclusions and morphological observation of metastable and stable pitting on stainless steel. *J. Electrochem. Soc.* **154**, C439–C444 (2007).

41. Suter, T., Peter, T. & Böhni, H. Microelectrochemical investigations of MnS inclusions. *Mater. Sci. Forum* **192-194**, 25–40 (1995).

42. Böhni, H., Suter, T. & Schreyer, A. Micro- and nanotechniques to study localized corrosion. *Electrochim. Acta* **40**, 1361–1368 (1995).

43. Shimahashi, N., Muto, I., Sugawara, Y. & Hara, N. Effects of corrosion and cracking of sulfide inclusions on pit initiation in stainless steel. *J. Electrochem. Soc.* **161**, C494–C500 (2014).

44. Webb, E. G. & Alkire, R. C. Pit initiation at single sulfide inclusions in stainless steel: III. Mathematical model. *J. Electrochem. Soc.* **149**, B286–B295 (2002).

45. Ryan, M. P., Williams, D. E., Chater, R. J., Hutton, B. M. & McPhail, D. S. Why stainless steel corrodes. *Nature* **415**, 770–774 (2002).

46. Suzuki, T., Yamabe, M. & Kitamura, Y. Composition of anolyte within pit anode of austenitic stainless steels in chloride solution. *Corrosion* **29**, 18–22 (1973).

47. Turnbull, A. The solution composition and electrode potential in pits, crevices and cracks. *Corros. Sci.* **23**, 833–870 (1983).

48. Kaji, T., Sekiai, T., Muto, I., Sugawara, Y. & Hara, N. Visualization of pH and pCl distributions: initiation and propagation criteria for crevice corrosion of stainless steel. *J. Electrochem. Soc.* **159**, C289–C297 (2012).

49. Nishimoto, M., Ogawa, J., Muto, I., Sugawara, Y. & Hara, N. Simultaneous visualization of pH and Cl⁻ distributions inside the crevice of stainless steel. *Corros. Sci.* **106**, 298–302 (2016).

50. Matsumura, K., Nishimoto, M., Muto, I. & Sugawara, Y. Sudden pH and Cl⁻ concentration changes during the crevice corrosion of type 430 stainless steel. *J. Electrochem. Soc.* **169**, 101506 (2022).

51. Suter, T., Webb, E. G., Böhni, H. & Alkire, R. C. Pit Initiation on stainless steels in 1 M NaCl with and without mechanical stress. *J. Electrochem. Soc.* **148**, B174–B185 (2001).

52. Brossia, C. S. & Kelly, R. G. Occluded solution chemistry control and the role of alloy sulfur on the initiation of crevice corrosion in type 304ss. *Corros. Sci.* **40**, 1851–1871 (1998).

53. Li, G. et al. Dissolution kinetics of the sulfide-oxide complex inclusion and resulting localized corrosion mechanism of X70 steel in deaerated acidic environment. *Corros. Sci.* **174**, 108815 (2020).

ACKNOWLEDGEMENTS

AUTHOR CONTRIBUTIONS
N.I.: investigation, methodology, data curation, visualization, writing—original draft. M.N. investigation, conceptualization, methodology, data curation, visualization, writing—review, and editing. I.M.: conceptualization, methodology, writing—review and editing, supervision, funding acquisition. Y.S.: writing—review and editing.

COMPETING INTERESTS

ADDITIONAL INFORMATION